Materials Horizons

ROYAL SOCIETY OF CHEMISTRY

COMMUNICATION

View Article Online
View Journal

Open Access Article. Published on 17 November 2025. Downloaded on 1/25/2026 3:07:40 PM.
This article is licensed under a Creative Commons Attribution-NonCommercial 3.0 Unported Licence.

Check for updates

Cite this: DOI: 10.1039/d5mh01939g

Received 14th October 2025,
Accepted 15th November 2025

DOI: 10.1039/d5mh01939g

rsc.li/materials-horizons

Charge state-dependent ion condensation near conjugated polymer backbones

Dilara Meli, †[ab] Quentin Thomas, †[c] Nicolas Rolland,[cd] Guillaume Freychet,[ef] Christina J. Kousseff,[g] Priscila Cavassin,[b] Lucas Q. Flagg,[h] Vincent Lemaur,[c] Abhijith Surendran,[i] Zeinab Hamid,[g] Sophie Griggs,[g] Ruiheng Wu,‡[bj] Rosalba A. Huerta,[ab] Isaiah D. Duplessis,[ab] Bryan D. Paulsen,[ik] Tobin J. Marks,[abjl] Lincoln J. Lauhon,[ab] Iain McCulloch,[gm] Lee J. Richter,[h] David Beljonne[c] and Jonathan Rivnay *[abi]

Despite the technological appeal of polymeric organic mixed ionic/electronic conductors (OMIECs) for diverse applications, a deep understanding of the fundamentals of mixed charge transport in these materials, especially regarding the complex interplay between polymer, ion and solvent structure in determining transport, is lacking. Herein, extensive molecular dynamics (MD) simulations of a model OMIEC representing various electrochemically gated states are reported that reveal charge state-dependent counterion condensation. X-ray diffraction simulations based on the MD data predict a measurable change in the scattering intensity at the counterion absorption edge, indicative of counterion repositioning with charging. We leverage an operando resonant X-ray scattering technique to experimentally corroborate the simulated scattering and report excellent agreement between predicted and experimental data, confirming that counterions preferentially reside in the lamellar mid-plane of crystallites at low doping, and near the polymer backbone at higher doping. Driving forces for ion type-dependent spatial repositioning and implications thereof are discussed.

New concepts

Gaining insight into the behavior of charge balancing counterions within mixed conducting systems has remained a significant technological challenge. We report here on the first *operando* measurement of counterion position within conjugated polymer crystallites. Notably, we find that instead of counterion size, polymer charge state and associated ion and water interactions dictate counterion location. Specifically, ions reside far away from the electronic charge transporting polymer backbone at low doping and migrate to positions near the backbone with increased charging.

Introduction

The study of charged polymer–ion interactions spans diverse classes of charged polymers (*e.g.*, polyelectrolytes, radical polymers, conjugated polymers) and carries broad implications, from elucidating biological processes such as protein folding to guiding the design of technology such as ion exchange resins and polymer batteries. One such class of polymers, organic mixed ionic/electronic conductors (OMIECs), comprise a broad library of materials that hold promise for myriad applications

[a] *Department of Materials Science and Engineering, Northwestern University, Evanston, Illinois 60208, USA. E-mail: jrivnay@northwestern.edu*
[b] *Northwestern University Materials Research Center, Evanston, Illinois, 60208, USA*
[c] *Laboratory for Chemistry of Novel Materials, Materials Research Institute, University of Mons, Mons, Belgium. E-mail: david.beljonne@umons.ac.be*
[d] *Université de Lille, CNRS, Centrale Lille, Univ. Artois, UMR 8181 – UCCS – Unité de Catalyse et Chimie du Solide, F-59000 Lille, France*
[e] *NSLS-II, Brookhaven National Laboratory, Upton, New York 11973, USA*
[f] *Univ. Grenoble Alpes, CEA, Leti, F-38000 Grenoble, France*
[g] *Department of Chemistry, Chemistry Research Laboratory, University of Oxford, Oxford, OX1 3TA, UK*
[h] *Materials Science and Engineering Division, National Institute of Standards and Technology, Gaithersburg, Maryland 20899, USA*
[i] *Department of Biomedical Engineering, Northwestern University, Evanston, Illinois 60208, USA*
[j] *Department of Chemistry, Northwestern University, Evanston, Illinois 60208, USA*
[k] *Department of Chemical and Biomolecular Engineering, University of Notre Dame, Notre Dame, IN 46556, USA*
[l] *Graduate Program in Applied Physics, Northwestern University, Evanston, Illinois 60208, USA*
[m] *Andlinger Center for Energy and the Environment, Department of Electrical and Computer Engineering, Princeton University, Princeton, NJ 08544, USA*
† These authors contributed equally.
‡ Current address: Department of Chemical Engineering, Stanford University, Stanford, California 94305, USA.

Open Access Article. Published on 17 November 2025. Downloaded on 1/25/2026 3:07:40 PM.
This article is licensed under a Creative Commons Attribution-NonCommercial 3.0 Unported Licence.

including neuromorphic devices, bioelectronic interfaces, and energy storage.[1–3] Conjugated polymer electrolytes are a subclass of OMIECs wherein uptake of ions facilitates injection of electronic charge carriers on π-conjugated polymer backbones enabling large transconductances at low doping potentials. In electrolyte-gated OMIECs, the development of a complete picture of fundamental charge transport and ion–electron interactions is complicated by the mobile nature of compensating charges (counterions),[4,5] thin film semi-crystallinity,[6] and doping induced nano- and mesoscale strains.[7,8] Gleaning information about ion behaviour in particular has proven challenging, although significant progress has been made in this area in recent years. On the modelling side, all-atom and coarse-grained molecular dynamics (MD) simulations have been applied to elucidate morphological changes induced by doping and/or de-doping in various conjugated polymer electrolytes. These include the swelling of a glycolated polythiophene (p(gT2)),[9] poly(3,4-ethylene dioxythiophene) Tosylate (PEDOT:Tos)[10] and poly(3,4-ethylene dioxythiophene) poly(styrene sulfonate) PEDOT:PSS,[11] the substrate-dependent structural phase transition in 2,5-bis-(thiophenyl)-1,4-bis(2-(2-(2-methoxyethoxy)ethoxy)-ethoxy)benzene (PB2T-TEG),[12] or the effect of various solvents, salts and salt concentrations on the microstructural features of poly(3,4-propylenedioxythiophene) (PProDOT).[13] Modelling has also predicted strong interactions of glycolated thiophenes with cations and water.[14,15] Experimentally, ion mobility has been measured directly on the device scale,[16] strongly affects device response time asymmetry,[17] and does not limit doping at low voltages.[18] It has also been shown that ions typically enter the film with an electrolyte concentration and ion type dependent hydration shell.[19,20] Experimental technique development has aided in improving the understanding of such processes, for example, *operando* nuclear magnetic resonance (NMR) has shed insight into charge coupling efficiency and local ion environments in PEDOT:PSS.[21] In addition, photoinduced force microscopy (PiFM) and photoluminescence have shown that, during charging, ions are initially injected into crystalline domains,[22,23] in agreement with the assumption that lower bandgap regions of the film are doped first.

Yet, knowledge about the precise location of ions is limited, especially with respect to electronic charge transporting conjugated polymer backbones. While some polymers are rigid-rod like and conduction is determined by short contacts,[24] most other OMIECs are semi-crystalline.[6] Therein, such aggregates and/or crystalline domains are a dominant contributor of the percolative charge transport network and may be leveraged to shed light on processes occurring in amorphous domains. It is essential to determine counterion position with respect to these ordered assemblies since the distance between the electronic and ionic charges strongly impacts interfacial capacitance and could create traps for hole/electron transport.[25] Despite the counterion-hole (or electron) separation being unknown, some synthetic design strategies presumed that it could strongly affect charge transport and that separating the holes/electrons from counter ions (*e.g.*, by adding alkyl spacers) could be a strategy towards improved performance.[26,27] Recently, it has been established that grazing incidence resonant X-ray diffraction (GIRXRD) can quantitatively determine the location of counter ions in a semicrystalline polymer OMIEC.[28] Initial *ex situ* (dry) measurements established that, counter to naïve expectation, the counter ion resides near the lamellar half-plane (far from the charge carrier). However, the *operando* state, where solvent swelling occurs, is vastly disparate in terms of polymer structure[29–31] and the dielectric environment of solvated ions; therefore, determining counterion position during operation is a critical need.

We report here on a novel MD model designed to closely replicate experimental *operando* doping conditions for a model semi-crystalline polymer OMIEC. To the best of our knowledge, no numerical simulations have yet been reported that replicate the experimental conditions of ion insertion and their spatial organization into crystalline domains as a function of electrical charging. Starting from a well-defined structure of the polymer crystallites, our MD simulations successfully capture the insertion of ions, surrounded by their hydration spheres, into the crystallites as a function of the doping state of the polymer backbones. We find that the average position of the ions with respect to the lamellae varies dramatically with degree of charging, exhibiting condensation near the backbone at high degrees of doping. We then generated synthetic grazing-incidence resonant X-ray diffraction (GIRXRD) data based on the MD simulations that show that counterion condensation near conjugated polymer backbones should be measurable. *Operando* GIRXRD experiments corroborate predicted results, showing excellent agreement between MD and experiment. The findings demonstrate that ion condensation is strongly influenced by the polymer's charge state and the nature of the anionic species. We marry the complementary approaches to both verify the interpretation of experimental data and to gain insights about ion–polymer interactions that were previously inaccessible. Finally, we leverage the MD simulations to gain mechanistic insight into the driving forces for ion condensation. This work thus emphasizes the importance of simulated data and suggests important implications for materials design and electrolyte choice in mixed conductors towards improved materials performance.

Computational insight into charged structures

Typically, when p-type accumulation mode OMIECs are oxidized, water and charge compensating anions are injected from surrounding electrolyte reservoirs into the polymer microstructure.[4,32] While the bulk of this swelling does not happen in the highly ordered regions of the polymer, some fraction of those ions and water will intercalate in the interlamellar space of crystallites.[5,30,33] The expansion of these regions can be measured with conventional monochromatic X-ray scattering, but information about where ions reside within the crystallites is inaccessible. However, since diffraction intensity is strongly influenced by atomic scattering factors, if the incident X-ray

Open Access Article. Published on 17 November 2025. Downloaded on 1/25/2026 3:07:40 PM.
This article is licensed under a Creative Commons Attribution-NonCommercial 3.0 Unported Licence.

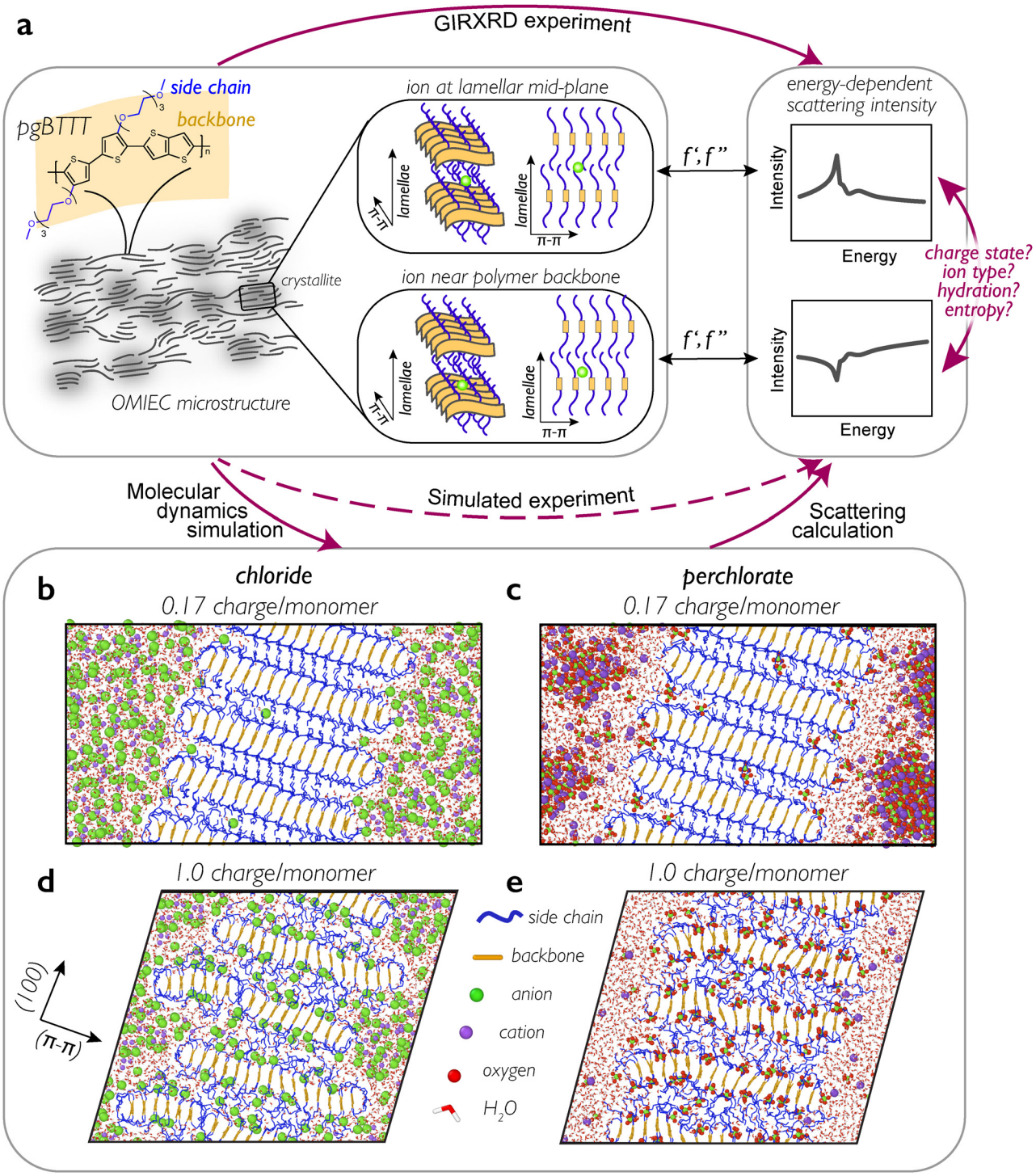

Fig. 1 (a) Left, schematic of OMIEC microstructure with hypothesized ion positions at the mid-plane and near the backbone. Inset shows pgBTTT chemical structure. Right, energy-dependent scattering intensity for the two proposed ion positions. Snapshots from MD simulations of polymer crystallites at 0.17 (b), (c) and 1.0 (d), (e) charge/monomer in NaCl (b), (d) and KClO4 (c), (e) electrolytes. Cl^- ions are shown in green, O atoms in red, cations (Na, K) in purple, ethylene glycol polymer side chains in blue, and thiophene–thienothiophene backbones in orange. The polymer backbone is in the out-of-page direction. The snapshots replicate one repeat of the simulation box in the (100) direction for clarity and were rendered using Ovito.[35]

energy is scanned across the absorption edge of a chemically differentiable counterion, diffraction (for example, in the (100), lamellar packing direction) will be modulated accordingly if the counterions are intercalated in the lamellae (Fig. 1(a)). Depending on the distance between the counterion and the polymer backbone, the incident energy dependence of the lamellar peak intensity takes on characteristic profiles indicative of their relative positions. This technique, known as

Open Access Article. Published on 17 November 2025. Downloaded on 1/25/2026 3:07:40 PM.
This article is licensed under a Creative Commons Attribution-NonCommercial 3.0 Unported Licence.

grazing-incidence resonant X-ray diffraction (GIRXRD), has been leveraged *ex situ* to show that ClO_4^- counterions reside near the lamellar half-plane regardless of doping state in a glycolated analogue of poly(3-hexylthiophene) (P3HT), poly(3-{[2-(2-methoxyethoxy)ethoxy]methyl}thiophene-2,5-diyl) (P3MEEMT).[28] This mid-plane observation is surprising, as it suggests a ≈0.9 nm separation between the holes on the backbone and their charge-coupled counterions, counterintuitive to what one might expect based on Coulombic attraction between the two charge carriers. We propose this organization results from the interplay between Coulombic forces bringing the ions close to the backbones and entropic forces favouring free-volume regions at end chains.

However, past experience has shown that both spectroscopic and structural characterization of OMIECs during operation do not agree with *ex situ* measurements, accordingly, we sought to understand ion–backbone interactions with MD and *operando* X-ray scattering. We chose the high-performing p-type OMIEC poly(2-(4,4′-bis(2-methoxyethoxy)-5′-methyl-[2,2′-bithiophen]-5-yl)-5-methylthieno[3,2-b]thiophene), pgBTTT,[34] shown as an inset in Fig. 1(a). pgBTTT is well studied compared to other OMIECs, stable for the duration of the experiment and exhibits robust out-of-plane lamellar scattering which simplifies the interpretation of the GIRXRD signal. First, MD simulations were initialized with crystallites consisting of two lamellae and a π-stack of 15 polymer chains, which is comparable to the size of experimentally observed crystallites (3–5 lamellae and 15–18 π-stacks). A dimer wide (box depth of two pgBTTT repeat units) section of the crystallite (total of 60 monomers) was surrounded by 4 mol L^{-1} electrolyte solution as seen in Fig. S1.[35] This electrolyte concentration was chosen to ensure doping within the timeframe accessible *via* MD, while preserving the structural organization in the small size crystalline models used. Attempts with low ionic concentration result in severe disruptions of the nanocrystals when the numerical doping speed exceeds the rate for ion transport and injection from the electrolyte solution into the films (because of transient excess of positive charges in the polymer). In real samples, these crystalline domains are embedded in amorphous regions acting as buffer layers for the ions and ensuring overall mechanical stability of the films in the doped state. Experimentally, it has been shown that at higher electrolyte concentrations counterions shed their hydration shells, which affects polymer swelling, leading to improved transconductances and switching times.[20] After equilibration, the atomic charges on the conjugated backbone were fractionally increased in six discrete steps and the charge equivalent number of cations were removed from the system (10 for each step). Herein, the implicit assumption is that the charge density is uniform within the crystallite and holes are fully delocalized across the backbone. While charge delocalization is conjugation length dependent, it is estimated that polarons are delocalized across ≈3–4 repeat units (12–16 thiophenes) in PBTTT,[36] the alkylated analogue to pgBTTT, which is larger than estimates in P3HT (5–7 thiophenes).[37]

With this procedure, we analysed 7 discrete charge states of the polymer: undoped (0 charge per monomer) and 0.17, 0.33, 0.5, 0.67, 0.83, and 1.0 charge per monomer (or per 4 thiophenes). Fig. 1(b)–(e) show MD snapshots of crystallites at two charge states (0.17 and 1.0 charge per monomer) in aqueous NaCl and $KClO_4$ solutions. Lamellae are clearly expanded to accommodate counterion and water injection. Counterions inserted into the lamellae closely match the number equivalent of holes distributed in the crystallite (Fig. 2(a), ≈10 for each charging step), though the number of compensating chloride anions is slightly smaller than perchlorate anions. This is possibly due to charge shielding effects imposed by the hydration shell around Cl^- anions, as evidenced by the fact that the largest disparity is during the first charging step, where the Cl^- to water ratio is largest (Fig. 2(b), >20 water molecules/Cl^-). As the polymer is further charged, the water to Cl^- ratio levels out to ≈13. In contrast, the ratio of water to perchlorate anions remains mostly constant for each charging state at 7–9 water molecules per anion. This results in a much larger lamellar expansion for Cl^- than ClO_4^- containing electrolytes (Fig. 2(c)). As seen in Tables S1 and S2, predicted crystallite swelling closely matches experimental values. As expected,

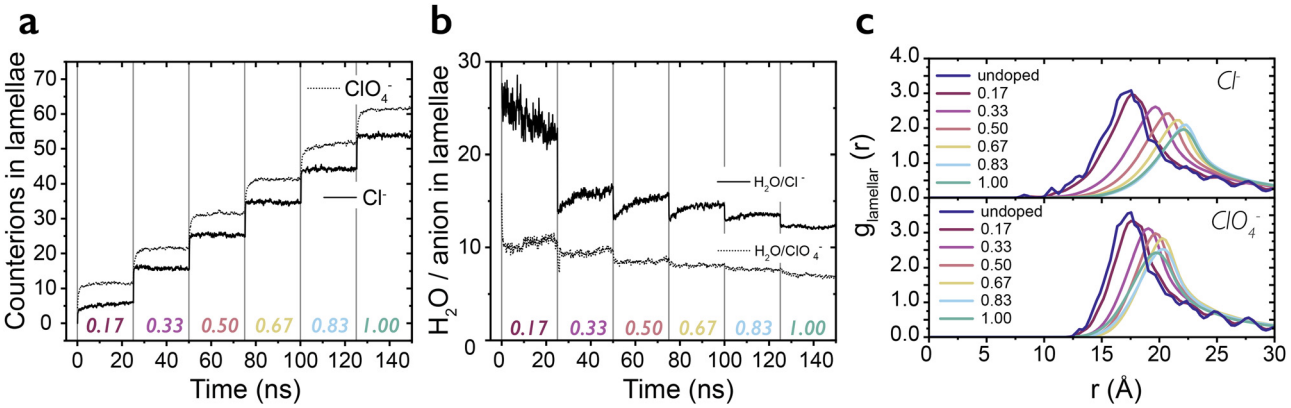

Fig. 2 (a) Counterions inserted between lamellae during sequential charging steps averaged across 25 simulation seeds. (b) Water to anion ratio during each charging step. (c) Radial distribution function of lamellae at each charge state for (top) chloride and (bottom) perchlorate electrolytes. Decimal fraction indicates relative charge per monomer (or 4 thiophenes).

Open Access Article. Published on 17 November 2025. Downloaded on 1/25/2026 3:07:40 PM.
This article is licensed under a Creative Commons Attribution-NonCommercial 3.0 Unported Licence.

experimentally measured crystallite spacings are slightly larger in the more dilute solvents due to the contribution of water (for a more detailed discussion on OMIEC swelling, see Section S1). It is worth noting here that while ensuing Cl^- GIRXRD experiments utilized KCl and MD calculations NaCl salts, we observed no participation of cations in the doping process (Fig. S2), which agrees with literature for Cl^- containing salts.[4]

Charge state-dependent counterion condensation

Mapping of the counterion distribution within the crystallites shows clear dependence of the preferential site with charge state (Fig. 3(a) and (b)). At low doping, ions preferentially reside at the polymer mid-plane but with increased charging they localize near the backbone. This is corroborated by radial distribution functions, $g(r)$, between counterions and sulfur atoms on the polymer backbone, which show broad distributions around the mid-plane at lower doping and ordering ≈ 4 Å at away from the backbone at higher doping (Fig. S3). Along the backbone direction, the preferential site for the condensed ions is on the opposite side of where the side chains are attached, near the sulfur atoms in the thiophene rings (Fig. 3(a), (b) and Fig. S3b–e, S4a–d).

Tracking the ions by preferred site in the lattice, it can be seen that the perchlorate anions condense at lower charge

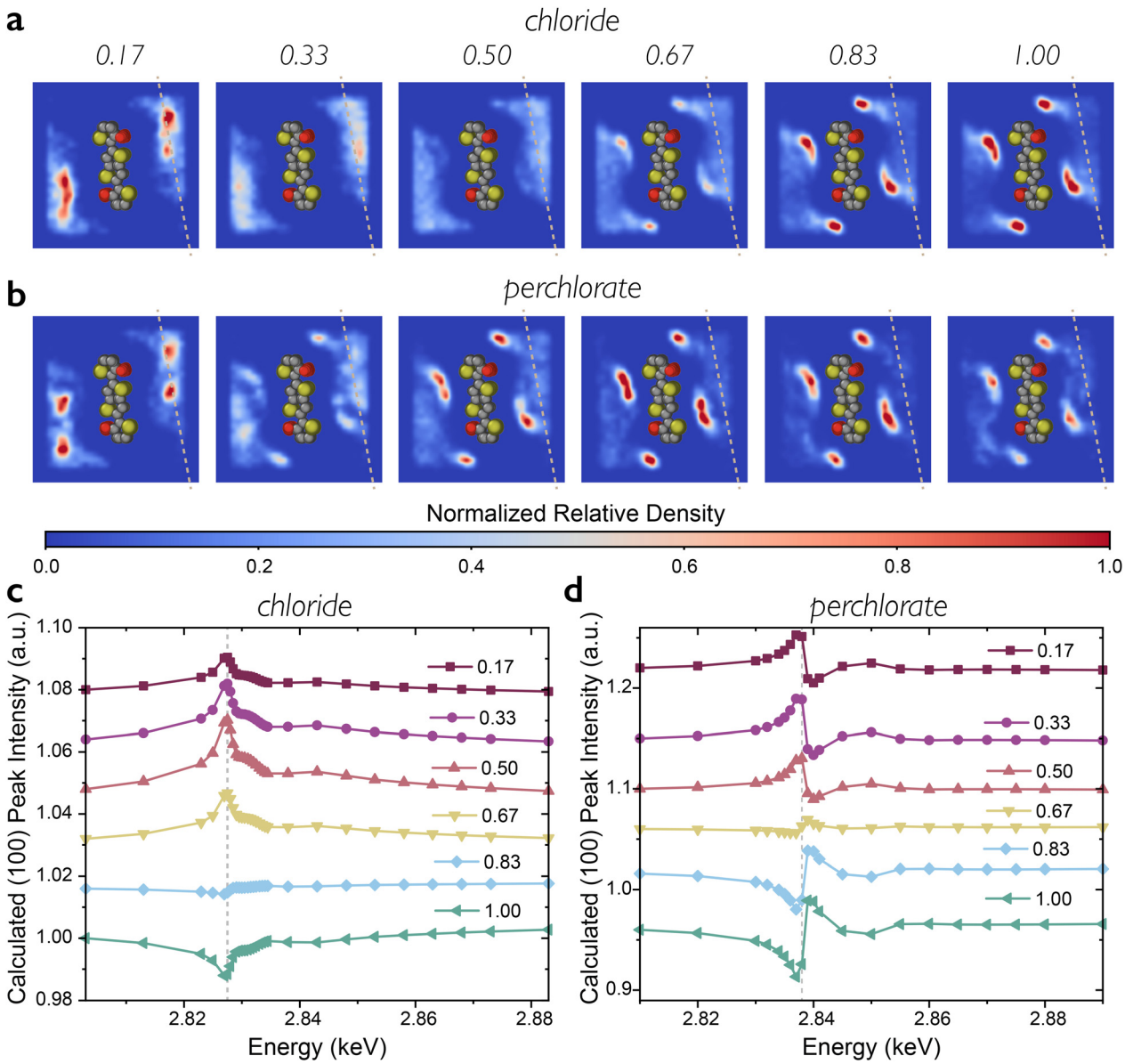

Fig. 3 (a) Averaged density maps of chloride and (b) perchlorate counterions in the vicinity of one pgBTTT repeat unit at each charge state. Sulfur atoms are shown in yellow, side chains are cropped for clarity and only the first oxygen is shown (red). Plots are normalized by the total density of ions at a given charge state. Dashed lines are a guide to the eye parallel to the backbone direction at the position of peak ion density at the low charging condition. Calculated lamellar (100) peak intensity as a function of energy for each charge state based on MD simulations of pgBTTT in (c) chloride and (d) perchlorate electrolytes. Dashed lines in (c) and (d) are guides to the eye. Decimal fractions indicate charge per monomer.

Open Access Article. Published on 17 November 2025. Downloaded on 1/25/2026 3:07:40 PM.
This article is licensed under a Creative Commons Attribution-NonCommercial 3.0 Unported Licence.

densities than the chloride anions (Fig. S5). It's possible that the less hydrated perchlorate anions experience greater electrostatic repulsion and thus reposition at lower doping. There are fewer side chain atoms to be found near chloride anions than perchlorate ions in the coordination shells we considered (4 Å and 6 Å), likely due to the larger number of water molecules surrounding chloride anions (Fig. S6). Both ions shed part of their outer hydration shell when they condense. Perhaps surprisingly, despite observed differences in the coordination environments of ions and their condensation behaviour, side chains behave similarly in both systems (Fig. S7).

To later compare these findings directly with experiments, GIRXRD data were simulated based on the MD structures (see Section S2). Specifically, lamellar diffraction peak intensities were computed as a function of energy for each charge state (Fig. 3(c) and (d)). The resonant diffraction signals of the chloride simulations first show a peak that grows in intensity (constructive interference) up to 0.5 charge per monomer, indicative of ions residing near the lamellar half-plane. After that, the signal gradually flips to a dip across the absorption edge (destructive interference) denoting a shift in ion location to positions near the polymer backbone. Calculations performed on perchlorate simulations show a similar flip in the nature of the Fano-like lineshape, where the intensity first increases, followed by a sharp dip and another increase (up-down-up). Once the ions condense, the phase of the interference in the signal changes to first show a dip, then a sharp increase followed by a taper back to baseline (down-up-down). As the density maps indicated, the flip in the signal happens at lower charge states in the perchlorate salt. These findings are robust across different simulation seeds (Fig. S8 and S9).

Operando experimental tracking of counterions

To experimentally corroborate predicted results, we adapted a previously published cell design that enables liquid electrolyte gating while bypassing deleterious scattering (Fig. 4(a) and Fig. S10).[29] Fig. 4(b) shows real (f') and imaginary (f'') parts of the Cl^- atomic scattering factor, extracted from background fluorescence of GIRXRD experiments, where the overlaid scatter plot highlights sampling of the incident energy across the Cl^- absorption edge (ClO_4^- atomic scattering factors can be found in Fig. S11). GIRXRD data were collected on a 2D detector and reduced to out-of-plane linecuts (Fig. S12 and S13). The peak around $q_z \approx 0.23$ Å^{-1} (≈ 0.3 Å^{-1} for $KClO_4$) is the (100) lamellar peak and the peak at ≈ 0.43 Å^{-1} is a scattering feature of the Kapton window of the cell that enables hydrated N_2 gas flow within a larger vacuum chamber. Spectroelectrochemical data for pgBTTT doped in KCl are shown in Fig. 4(c). To investigate the counterion localization as a function of charge state, we focused our experiments on three doping states: de-doped (−250 mV), mid-doped (+250 mV) and highly doped (+750 mV *vs.* Ag/AgCl). At the de-doped potential, the spectrum shows a clear neutral pgBTTT absorption band, related to the π–π* transition, around 620 nm.[34] At the mid-doped potential, the neutral absorption decreases with a concomitant increase in the singly charged (polaronic) ($\approx$930 nm) and doubly charged (bipolaronic) ($\approx$1150 nm) regions.[38] At the highly doped potential, the spectrum shows almost complete bleaching of the neutral absorption peak, depletion of the polaronic band and an increase of the bipolaronic band, which is an indication of the interconversion of polaronic into bipolaronic carriers. Similar to other systems,[33] lamellar diffraction of pgBTTT gated in KCl is highly charge state-dependent where increased doping leads to an increase in spacing and coherence (Fig. S12). Unfortunately, the loss of order in the de-doped states leads to inaccessibility of the resonant diffraction signal. By fitting the out-of-plane lamellar diffraction peak (sample fit shown in Fig. S14), it is apparent that when charged to the mid-doped state, lamellar diffraction as a function of incident energy is largely unchanged when scanned across the absorption edge, whereas the highly doped sample shows a clear dip (Fig. 4(d)). For comparison, the background intensity has the same shape as f'' (Fig. S15). The absence of a clear dip in the mid-doped state can be interpreted as either ordering of the counterions between the half-plane and near positions or an averaging of signals from crystallites with ions ordered in either the near or far positions. The signal at high doping matches with the predicted GIRXRD signal from MD, indicative of ordering of the counterion near the backbone.

In comparison with chloride, perchlorate anions appear to dope the polymer more readily as seen in the shifted threshold voltage in the spectroelectrochemistry (Fig. 4(e) and Fig. S16). Aside from the shift in voltage, the optical spectra are similar. In comparison with the lamellar expansion in KCl, pgBTTT doped in KClO4 expands much less during doping but also shows enhanced ordering at increased bias (Fig. S13). Averaging linecuts at two mid-doping potentials, the GIRXRD signal takes on the predicted up-down-up shape, confirming ordering at the mid-plane (Fig. 4(f)). At high doping, the counterions condense causing a flip in the signal to the down-up-down shape (Fig. 4(f)), again matching the calculations based on the MD.

As in the previous GIRXRD study,[28] *ex situ* experiments on pgBTTT films doped in 0.1 mol L^{-1} $KClO_4$ at +600 mV *vs.* Ag/AgCl show that the counterions are ordered near the lamellar half-plane at high doping (Fig. S17). The main difference between *ex situ* and *operando* experiments is the removal of most of the water in the lattice in the former. To probe its role in facilitating counterion condensation, we conducted the *ex situ* experiment in a high humidity environment (see Section S3). The results show that the counterions remain at the mid-plane in a less doped film but condense with vapor swelling in a highly doped film. However, we emphasize the vital role of *operando* experiments in capturing transport-critical structural nuance in OMIECs since the ability to maintain a doped state *ex situ* is electrolyte-dependent and the vapor swelling behaviour of some polymers can be significantly different than their *operando* swelling.[30] Although we have confirmed charge state-dependent counterion condensation experimentally, direct matching of results from MD and doping states measured experimentally is difficult. While the bulk charge

Open Access Article. Published on 17 November 2025. Downloaded on 1/25/2026 3:07:40 PM.
This article is licensed under a Creative Commons Attribution-NonCommercial 3.0 Unported Licence.

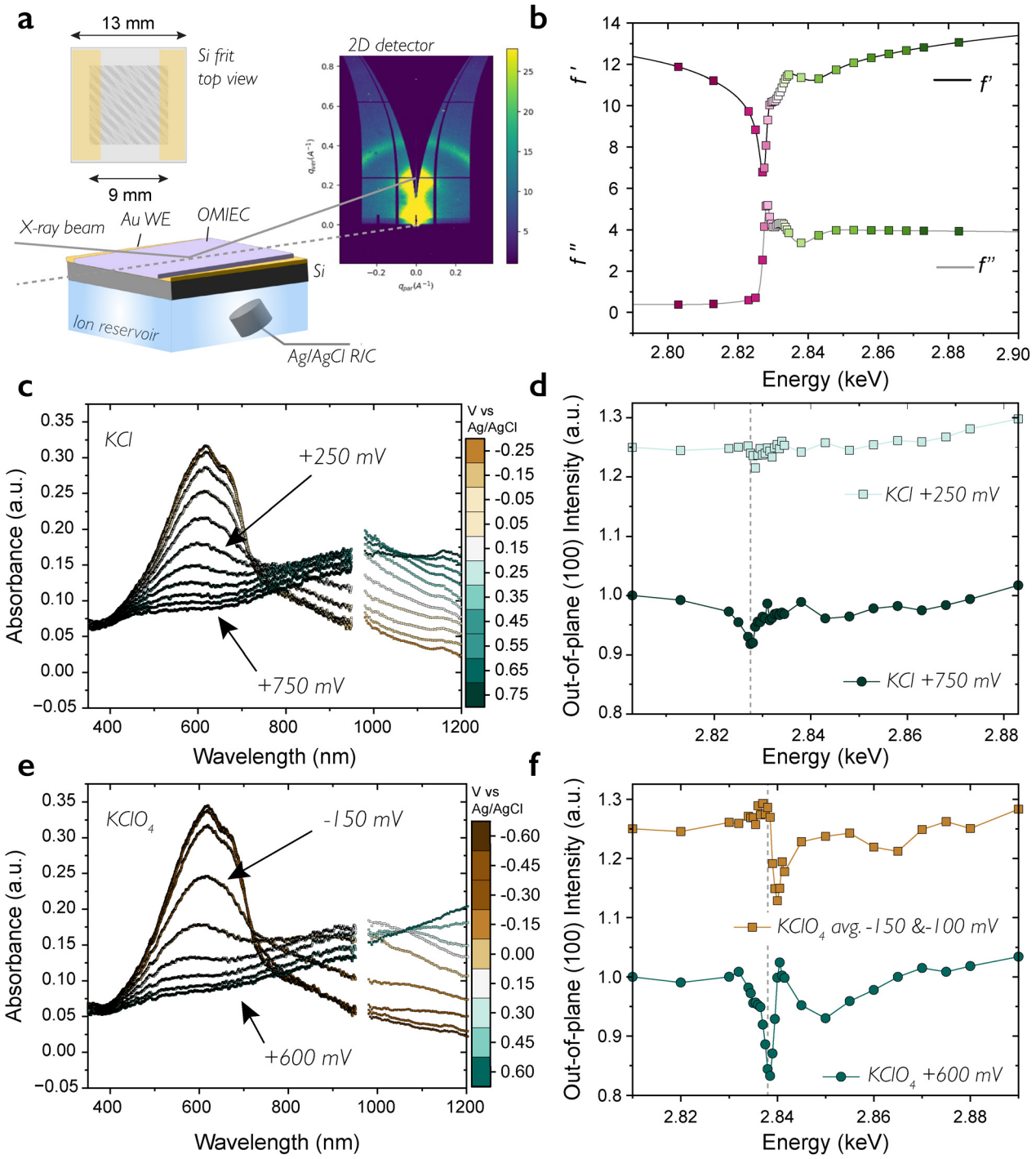

Fig. 4 (a) Schematic of the operando GIRXRD experimental setup where the OMIEC is separated from the electrolyte through a porous Si wafer. Inset shows top view of the Si wafer with separated Au working electrodes. (b) Real (f') and imaginary (f'') atomic scattering factors of Cl^- extracted from background fluorescence. (c) Spectroelectrochemical data of pgBTTT gated in 0.1 mol L^{-1} KCl electrolyte with neutral pgBTTT (≈620 nm), polaronic (≈930 nm) and bipolaronic (≈1150 nm) bands. The region around 980 nm could not be measured (change over from visible to near infrared detector). (d) Out of-plane lamellar peak intensity for mid-doped (+250 mV) and highly doped (+750 mV *vs.* Ag/AgCl) pgBTTT in 0.1 mol L^{-1} KCl. (e) Spectroelectrochemical data of pgBTTT gated in 0.1 mol L^{-1} $KClO_4$ electrolyte. (f) Out of-plane lamellar peak intensity for mid-doped (averaged −150 and −100 mV) and highly doped (+600 mV *vs.* Ag/AgCl) pgBTTT in 0.1 mol L^{-1} $KClO_4$. Dashed lines in (d) and (f) are a guide to the eye.

in a film can be estimated, partitioning charge between the crystalline and amorphous regions is difficult.[39] Additionally, OMIECs gated in aqueous electrolytes are prone to side reactions[40] and are often ambiently doped.[41]

Open Access Article. Published on 17 November 2025. Downloaded on 1/25/2026 3:07:40 PM.
This article is licensed under a Creative Commons Attribution-NonCommercial 3.0 Unported Licence.

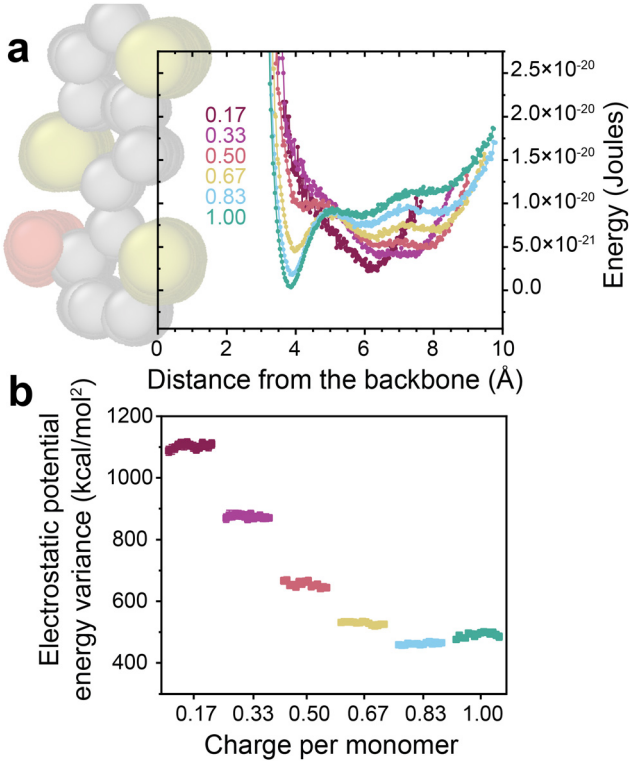

Fig. 5 (a) Energetic landscape felt by Cl^- ions in the lamellae. Snippet of polymer backbone for scale, data are cropped at the lamellar mid-plane. Decimal fraction indicates charge per monomer. (b) Electrostatic disorder in the central chains of the Cl^- doped lamellae, quantified by spatial variance as a function of doping step. For each 1-ns window, the per-site electrostatic energy was time-averaged and its variance across backbone sites was computed for the three central chains within the lamellae. The 15 equilibrated windows (within each 25-ns stage) are plotted consecutively.

Driving forces for condensation and implications for charge transport

Counterions reposition due to a change in the energetic landscape with doping (Fig. 5(a) and Fig. S18). At low doping and *ex situ*, side chains preserve some degree of order closer to the backbone (Fig. 1(b), (c) and Fig. S7). We propose that this leaves room at the mid-plane for counterions with many available sites and as such the energetic wells are broader due to higher configurational entropy of the ions. The wells show minima near the end of the side chains. With increased charging, more water and ions enter the interlamellar space, disrupting side chain order. This suggests that a reduced entropic contribution, in addition to the increased counterion repulsion, drives the ions away from the mid-plane closer to the oppositely charged backbones. This explanation is consistent with vapor experiments, where the addition of water vapor could aid in side chain disordering, facilitating the movement of ions to the different site.

The proximity of counterions to the holes on the polymer backbone has two competing effects on electronic charge transport. On the one hand, closer ions yield larger electrostatic energy gains, which can act as traps for holes, an effect that is exacerbated by the reduced hydration associated with ion condensation. On the other hand, as suggested by the narrower free energy well at high *versus* low doping (Fig. 5(a) and Fig. S18a), counterions adopt a more ordered arrangement at high doping levels, which can reduce energetic disorder in the electrostatic landscape. The latter effect appears to dominate: calculations of the spatial inhomogeneity of the electrostatic potential show that the variance of the mean potential on the central chains of the lamellae decreases by a factor of ≈ 2 when the doping increases from 0.17 to 1.00 charges per monomer (Fig. 5(b) and Fig. S18b). From a purely electrostatic standpoint, therefore, ion clustering near the backbone at high doping is not detrimental to charge transport. This conclusion is consistent with earlier studies of ion-exchange doping in crystalline PBTTT using ionic liquids,[42] where wide-angle X-ray scattering revealed that ionic liquid anions intercalate between side chains and reside in close proximity to the conjugated backbone. The near co-crystalline arrangement was shown to suppress Coulomb trapping of holes, as overlapping ion potential wells merged into a smooth energy landscape. Of course, this argument is limited to electrostatics. Other factors, such as positional or conformational disorder, may counteract the reduction in electrostatic disorder at high doping. In addition, electron–electron interactions coupled with disorder can give rise to a Coulomb gap that suppresses hole mobility.[43] Beyond mobility, changes in the preferred counterion site are expected to affect the molecular-scale capacitance.

These results highlight the need for deliberate materials design, where the interplay of backbone, side chain, and electrolyte (salt and solvent) selection governs ion condensation. Understanding counterion condensation is therefore critical not only for organic and hybrid MIECs in transistors and circuits, but also for applications in bioelectronics, soft robotics, neuromorphic devices, thermoelectrics, and energy storage.

Conclusions

In summary, we demonstrated the first *operando* measurement of counterion positions within OMIEC crystallites, revealing that they are not predicated by the ion size, rather, it is the interplay between the water and ions in the lattice and the charge on the polymer that dictate energetically favourable positions. Specifically, we showed that two counterions (Cl^- and ClO_4^-) condense near pgBTTT backbones with increased doping. This phenomenon could not be captured *ex situ* emphasizing the need for experiments that mimic the dynamic nature of these materials in their device-relevant operating state. The simulations indicate clear charge state dependence of counterion positions within the lattice, near the lamellar mid-plane at low doping and ≈ 4 Å away from the backbone at high doping. The MD data were then used to generate synthetic GIRXRD data, physically grounding the interpretation of experimental results. We find that the more chaotropic ClO_4^- anion condenses at lower doping potentials

Open Access Article. Published on 17 November 2025. Downloaded on 1/25/2026 3:07:40 PM.
This article is licensed under a Creative Commons Attribution-NonCommercial 3.0 Unported Licence.

than Cl^-. While the impact of this physical phenomenon on electronic charge transport remains unknown, the measurement capabilities and workflow demonstrated herein will ultimately be a crucial component of a detailed exploration on the relative effects of ion condensation, band-filling, and structural effects in limiting hole mobility at high doping potentials.

The key limitation of GIRXRD is that it only probes crystalline domains. However, it is likely that phenomena of counterion condensation translate to non-crystalline regions and systems, if there is sufficient confinement. In the future, these measurements should be extended to non-aqueous systems to access a wider voltage window, electron transporting materials to investigate cation/OMIEC and cation/electron interactions, as well as additional p-type systems to probe the effects of side chain design (*e.g.*, density, moieties). Finally, this work highlights how the union of experiment and theory can both ground interpretations and enable added atomistic insights that are (at present) not experimentally observable.

Materials and methods

Materials and methods are described in detail in Section S4.

Notes

Certain equipment, instruments, software, or materials are identified in this paper in order to specify the experimental procedure adequately. Such identification is not intended to imply recommendation or endorsement of any product or service by NIST, nor is it intended to imply that the materials or equipment identified are necessarily the best available for the purpose.

Author contributions

D. M., Q. T., N. R., V. L., B. D. P., D. B., and J. R. conceptualized this study. Q. T. performed and analysed MD calculations. V. L. parametrized the forcefield and identified the most stable structures for MD calculations. D. M., G. F., L. Q. F., P. C., I. D. D. and L. J. R. conducted operando GIRXRD experiments at NSLS-II. D. M. conducted analysis of operando GIRXRD experiments with the help of G. F. and L. J. R. who wrote analysis scripts. A. S. fabricated substrates for operando GIRXRD experiments and L. Q. F. designed the cell. G. F. conducted *ex situ* GIRXRD experiments. D. M. ran GIRXRD calculations on MD datasets with input from L. J. R. C. J. K., Z. H. and S. G. synthesized polymers for this study. D. M., R.W. and R. A. H. conducted hard X-ray GIWAXS experiments at SLAC. P.C. conducted and analysed spectroelectrochemistry experiments. T. J.M., L. J. L., I. M., D. B. and J. R. supervised trainees that contributed to this study.

Conflicts of interest

There are no conflicts to declare.

Data availability

All data and analysis scripts pertaining to this manuscript are available in the Dryad repository at **https://doi.org/10.5061/dryad.b8gtht7q0**.

Supplementary information (SI): supplementary notes 1–4, supplementary figures 1–21, and supplementary tables 1–2. See DOI: **https://doi.org/10.1039/d5mh01939g**.

Acknowledgements

This work was financially supported by the National Science Foundation's Materials Research Science Engineering Center (NSF DMR-2308691). This work made use of the NUFAB facility of Northwestern University's NUANCE Center, which has received support from the SHyNE Resource (NSF ECCS-2025633), the IIN, and Northwestern's Materials Research and Engineering Center (MRSEC) program (NSF DMR-2308691). The authors would like to thank Christopher J. Takacs, Patryk Wasik, and Eliot Gann for beamline support. This research utilized beamline 12-ID (SMI) of the national Synchrotron Light Source II, a US Department of Energy (DOE) Office of Science User Facility operated for the DOE Office of Science by Brookhaven National Laboratory under contract No. DE-SC0012704 and beamline 17-2 of the Stanford Synchrotron Radiation Lightsource (SSRL), SLAC National Accelerator Laboratory which is supported by the DOE, Office of Science, Office of Basic Energy Sciences under Contract No. DE-AC02-76SF00515. The work in Mons has received funding from the European Commission Horizon 2020 Future and Emerging Technologies (FET) project MITICS (964677) and the computational resources are supported by the FNRS "Consortium des Equipements de Calcul Intensif-CECI" program Grant No. 2.5020.11. Q. T. is FRIA grant holder from the Belgian National Fund for Scientific Research (FRS-FNRS). D.B. is FNRS Research Director. D.M. thanks Claire Donahue for fruitful discussions of NEXAFS data analysis.

References

1 Y. Yao, R. M. Pankow, W. Huang, C. Wu, L. Gao, Y. Cho, J. Chen, D. Zhang, S. Sharma, X. Liu, Y. Wang, B. Peng, S. Chung, K. Cho, S. Fabiano, Z. Ye, J. Ping, T. J. Marks and A. Facchetti, *Proc. Natl. Acad. Sci. U. S. A.*, 2025, **122**, e2414879122.
2 B. D. Paulsen, K. Tybrandt, E. Stavrinidou and J. Rivnay, *Nat. Mater.*, 2020, **19**, 13–26.
3 Y. Yao, W. Huang, J. Chen, X. Liu, L. Bai, W. Chen, Y. Cheng, J. Ping, T. J. Marks and A. Facchetti, *Adv. Mater.*, 2023, **35**, 2209906.
4 L. Q. Flagg, C. G. Bischak, R. J. Quezada, J. W. Onorato, C. K. Luscombe and D. S. Ginger, *ACS Mater. Lett.*, 2020, **2**, 254–260.
5 J. Tropp, D. Meli, R. Wu, B. Xu, S. B. Hunt, J. D. Azoulay, B. D. Paulsen and J. Rivnay, *ACS Mater. Lett.*, 2023, **5**, 1367–1375.
6 J. Rivnay, S. C. B. Mannsfeld, C. E. Miller, A. Salleo and M. F. Toney, *Chem. Rev.*, 2012, **112**, 5488–5519.

Open Access Article. Published on 17 November 2025. Downloaded on 1/25/2026 3:07:40 PM.
This article is licensed under a Creative Commons Attribution-NonCommercial 3.0 Unported Licence.

7 R. Wu, D. Meli, J. Strzalka, S. Narayanan, Q. Zhang, B. D. Paulsen, J. Rivnay and C. J. Takacs, *Nat. Mater.*, 2024, **23**, 648–655.
8 Y. Tsarfati, K. C. Bustillo, B. H. Savitzky, L. Balhorn, T. J. Quill, A. Marks, J. Donohue, S. E. Zeltmann, C. J. Takacs, A. Giovannitti, I. McCulloch, C. Ophus, A. M. Minor and A. Salleo, *Nat. Mater.*, 2025, **24**, 101–108.
9 J. Gladisch, E. Stavrinidou, S. Ghosh, A. Giovannitti, M. Moser, I. Zozoulenko, I. McCulloch and M. Berggren, *Adv. Sci.*, 2020, **7**, 1901144.
10 N. Delavari, J. Gladisch, I. Petsagkourakis, X. Liu, M. Modarresi, M. Fahlman, E. Stavrinidou, M. Linares and I. Zozoulenko, *Macromolecules*, 2021, **54**, 6552–6562.
11 M. Modarresi, A. Mehandzhiyski, M. Fahlman, K. Tybrandt and I. Zozoulenko, *Macromolecules*, 2020, **53**, 6267–6278.
12 S. Ghosh and I. Zozoulenko, *ACS Appl. Electron. Mater.*, 2020, **2**, 4034–4041.
13 X. Yang, H. Sun, X. He and K. Zhao, *Macromolecules*, 2025, **58**, 45–60.
14 M. Matta, R. Wu, B. D. Paulsen, A. J. Petty, R. Sheelamanthula, I. McCulloch, G. C. Schatz and J. Rivnay, *Chem. Mater.*, 2020, **32**, 7301–7308.
15 N. Siemons, D. Pearce, C. Cendra, H. Yu, S. M. Tuladhar, R. K. Hallani, R. Sheelamanthula, G. S. LeCroy, L. Siemons, A. J. P. White, I. McCulloch, A. Salleo, J. M. Frost, A. Giovannitti and J. Nelson, *Adv. Mater.*, 2022, **34**, 2204258.
16 R. Wu, X. Ji, Q. Ma, B. D. Paulsen, J. Tropp and J. Rivnay, *Sci. Adv.*, 2024, **10**(17), DOI: **10.1126/sciadv.adn8628**.
17 J. Guo, S. E. Chen, R. Giridharagopal, C. G. Bischak, J. W. Onorato, K. Yan, Z. Shen, C.-Z. Li, C. K. Luscombe and D. S. Ginger, *Nat. Mater.*, 2024, **23**, 656–663.
18 S. T. Keene, J. E. M. Laulainen, R. Pandya, M. Moser, C. Schnedermann, P. A. Midgley, I. McCulloch, A. Rao and G. G. Malliaras, *Nat. Mater.*, 2023, **22**, 1121–1127.
19 C. Cendra, A. Giovannitti, A. Savva, V. Venkatraman, I. McCulloch, A. Salleo, S. Inal and J. Rivnay, *Adv. Funct. Mater.*, 2019, **29**, 1807034.
20 A. Savva, C. Cendra, A. Giugni, B. Torre, J. Surgailis, D. Ohayon, A. Giovannitti, I. McCulloch, E. Di Fabrizio, A. Salleo, J. Rivnay and S. Inal, *Chem. Mater.*, 2019, **31**, 927–937.
21 D. Lyu, Y. Jin, P. C. M. M. Magusin, S. Sturniolo, E. W. Zhao, S. Yamamoto, S. T. Keene, G. G. Malliaras and C. P. Grey, *Nat. Mater.*, 2023, **22**, 746–753.
22 S. R. Jackson, R. L. Kingsford, G. W. Collins and C. G. Bischak, *Chem. Mater.*, 2023, **35**, 5392–5400.
23 G. W. Collins, M. S. Lone, S. R. Jackson, J. N. Keller, R. L. Kingsford, R. Noriega and C. G. Bischak, *Adv. Funct. Mater.*, 2024, 2403710.
24 J. F. Coker, S. Moro, A. S. Gertsen, X. Shi, D. Pearce, M. P. Van Der Schelling, Y. Xu, W. Zhang, J. W. Andreasen, C. R. Snyder, L. J. Richter, M. J. Bird, I. McCulloch, G. Costantini, J. M. Frost and J. Nelson, *Proc. Natl. Acad. Sci. U. S. A.*, 2024, **121**, e2403879121.
25 K. G. Cho, D. Z. Adrahtas, K. H. Lee and C. D. Frisbie, *Adv. Funct. Mater.*, 2023, **33**, DOI: **10.1002/adfm.202303700**.
26 Y. He, N. A. Kukhta, A. Marks and C. K. Luscombe, *J. Mater. Chem. C*, 2022, **10**, 2314–2332.
27 H. Yu, A. Marks, S. M. Tuladhar, N. Siemons, I. Anderson, S. Bidinger, S. T. Keene, T. J. Quill, R. Wu, O. Gough, G. Wu, F. Eisner, A. Salleo, J. Rivnay, G. G. Malliaras, P. R. F. Barnes, I. McCulloch and J. Nelson, *Angew. Chem., Int. Ed.*, 2024, e202417897.
28 L. Q. Flagg, J. W. Onorato, C. K. Luscombe, V. Bhat, C. Risko, B. Levy-Wendt, M. F. Toney, C. R. McNeill, G. Freychet, M. Zhernenkov, R. Li and L. J. Richter, *Chem. Mater.*, 2023, **35**, 3960–3967.
29 B. D. Paulsen, A. Giovannitti, R. Wu, J. Strzalka, Q. Zhang, J. Rivnay and C. J. Takacs, *Small*, 2021, **17**, 2103213.
30 L. Q. Flagg, L. E. Asselta, N. D'Antona, T. Nicolini, N. Stingelin, J. W. Onorato, C. K. Luscombe, R. Li and L. J. Richter, *ACS Appl. Mater. Interfaces*, 2022, **14**, 29052–29060.
31 T. J. Quill, G. LeCroy, D. M. Halat, R. Sheelamanthula, A. Marks, L. S. Grundy, I. McCulloch, J. A. Reimer, N. P. Balsara, A. Giovannitti, A. Salleo and C. J. Takacs, *Nat. Mater.*, 2023, **22**, 362–368.
32 J. Rivnay, S. Inal, A. Salleo, R. M. Owens, M. Berggren and G. G. Malliaras, *Nat. Rev. Mater.*, 2018, **3**, 1–14.
33 T. J. Quill, G. LeCroy, A. Marks, S. A. Hesse, Q. Thiburce, I. McCulloch, C. J. Tassone, C. J. Takacs, A. Giovannitti and A. Salleo, *Adv. Mater.*, 2024, **36**, 2310157.
34 R. K. Hallani, B. D. Paulsen, A. J. Petty, R. Sheelamanthula, M. Moser, K. J. Thorley, W. Sohn, R. B. Rashid, A. Savva, S. Moro, J. P. Parker, O. Drury, M. Alsufyani, M. Neophytou, J. Kosco, S. Inal, G. Costantini, J. Rivnay and I. McCulloch, *J. Am. Chem. Soc.*, 2021, **143**, 11007–11018.
35 A. Stukowski, *Modell. Simul. Mater. Sci. Eng.*, 2010, **18**, 015012.
36 R. Steyrleuthner, Y. Zhang, L. Zhang, F. Kraffert, B. P. Cherniawski, R. Bittl, A. L. Briseno, J.-L. Bredas and J. Behrends, *Phys. Chem. Chem. Phys.*, 2017, **19**, 3627–3639.
37 D. A. Stanfield, Z. Mehmedović and B. J. Schwartz, *Chem. Mater.*, 2021, **33**, 8489–8500.
38 I. Enokida and Y. Furukawa, *Org. Electron.*, 2019, **68**, 28–34.
39 P. Cavassin, I. Holzer, D. Tsokkou, O. Bardagot, J. Réhault and N. Banerji, *Adv. Mater.*, 2023, **35**, 2300308.
40 J. Guo, L. Q. Flagg, D. K. Tran, S. E. Chen, R. Li, N. B. Kolhe, R. Giridharagopal, S. A. Jenekhe, L. J. Richter and D. S. Ginger, *J. Am. Chem. Soc.*, 2023, **145**, 1866–1876.
41 A. Paterson, V. Le, K. N. B. K. N. Baustert, M. Brown, J. Bombile, L. Flagg, K. Thorley, C. Kousseff, O. Solomeshch, I. McCulloch, N. Tessler, C. Risko and K. Graham, 2024, DOI: **10.21203/rs.3.rs-4224356/v1**.
42 I. E. Jacobs, G. D'Avino, V. Lemaur, Y. Lin, Y. Huang, C. Chen, T. F. Harrelson, W. Wood, L. J. Spalek, T. Mustafa, C. A. O'Keefe, X. Ren, D. Simatos, D. Tjhe, M. Statz, J. W. Strzalka, J.-K. Lee, I. McCulloch, S. Fratini, D. Beljonne and H. Sirringhaus, *J. Am. Chem. Soc.*, 2022, **144**, 3005–3019.
43 D. H. L. Tjhe, X. Ren, I. E. Jacobs, G. D'Avino, T. B. E. Mustafa, T. G. Marsh, L. Zhang, Y. Fu, A. E. Mansour, A. Opitz, Y. Huang, W. Zhu, A. H. Unal, S. Hoek, V. Lemaur, C. Quarti, Q. He, J.-K. Lee, I. McCulloch, M. Heeney, N. Koch, C. P. Grey, D. Beljonne, S. Fratini and H. Sirringhaus, *Nat. Mater.*, 2024, **23**(12), 1712–1719, DOI: **10.1038/s41563-024-01953-6**.